

## MIT Open Access Articles

*Colossal oxygen vacancy formation at a fluorite-bixbyite interface*

The MIT Faculty has made this article openly available. **Please share** how this access benefits you. Your story matters.

**Citation:** Lee, Dongkyu et al. "Colossal oxygen vacancy formation at a fluorite-bixbyite interface." Nature Communications, 11, 1 (March 2020): 1371 © 2020 The Author(s)

**As Published:** 10.1038/S41467-020-15153-8

**Publisher:** Springer Science and Business Media LLC

**Persistent URL:** <https://hdl.handle.net/1721.1/126752>

**Version:** Final published version: final published article, as it appeared in a journal, conference proceedings, or other formally published context

**Terms of use:** Creative Commons Attribution 4.0 International license













## ARTICLE


<https://doi.org/10.1038/s41467-020-15153-8>

OPEN

# Colossal oxygen vacancy formation at a fluorite-bixbyite interface

Dongkyu Lee <sup>1,6,8</sup>, Xiang Gao<sup>1,7,8</sup>, Lixin Sun<sup>2</sup>, Youngseok Jee<sup>3</sup>, Jonathan Poplawsky <sup>1</sup>, Thomas O. Farmer<sup>1</sup>, Lisha Fan <sup>1</sup>, Er-Jia Guo <sup>1</sup>, Qiyang Lu <sup>2</sup>, William T. Heller <sup>1</sup>, Yongseong Choi <sup>4</sup>, Daniel Haskel<sup>4</sup>, Michael R. Fitzsimmons<sup>1,5</sup>, Matthew F. Chisholm<sup>1</sup>, Kevin Huang <sup>3</sup>, Bilge Yildiz <sup>2</sup> & Ho Nyung Lee <sup>1</sup>✉

Oxygen vacancies in complex oxides are indispensable for information and energy technologies. There are several means to create oxygen vacancies in bulk materials. However, the use of ionic interfaces to create oxygen vacancies has not been fully explored. Herein, we report an oxide nanobrush architecture designed to create high-density interfacial oxygen vacancies. An atomically well-defined (111) heterointerface between the fluorite CeO<sub>2</sub> and the bixbyite Y<sub>2</sub>O<sub>3</sub> is found to induce a charge modulation between Y<sup>3+</sup> and Ce<sup>4+</sup> ions enabled by the chemical valence mismatch between the two elements. Local structure and chemical analyses, along with theoretical calculations, suggest that more than 10% of oxygen atoms are spontaneously removed without deteriorating the lattice structure. Our fluorite-bixbyite nanobrush provides an excellent platform for the rational design of interfacial oxide architectures to precisely create, control, and transport oxygen vacancies critical for developing ionotronic and memristive devices for advanced energy and neuromorphic computing technologies.

<sup>1</sup>Oak Ridge National Laboratory, Oak Ridge, TN 37831, USA. <sup>2</sup>Laboratory for Electrochemical Interface, Department of Nuclear Science and Engineering, Massachusetts Institute of Technology, 77 Massachusetts Avenue, 24-210, Cambridge, MA 02139, USA. <sup>3</sup>Department of Mechanical Engineering, University of South Carolina, Columbia, SC 29208, USA. <sup>4</sup>Advanced Photon Source, Argonne National Laboratory, Argonne, IL 60439, USA. <sup>5</sup>Department of Physics and Astronomy, University of Tennessee at Knoxville, Knoxville, TN 37996, USA. <sup>6</sup>Present address: Department of Mechanical Engineering, University of South Carolina, Columbia, SC 29208, USA. <sup>7</sup>Present address: Center for High Pressure Science and Technology Advanced Research, Beijing, China. <sup>8</sup>These authors contributed equally: Dongkyu Lee, Xiang Gao. ✉email: [hnlee@ornl.gov](mailto:hnlee@ornl.gov)

Owing to the critical role of tunable oxygen defects, mixed ionic and electronic conducting oxides have become key components in many energy technologies, including energy conversion and generation<sup>1</sup>, solar hydrogen production<sup>2</sup>, humidity/gas detection<sup>3</sup>, and catalytic conversion of toxic species in automobile exhausts<sup>4</sup>. In particular, ceria ( $\text{CeO}_2$ ) has attracted extensive attention for its good ionic conductivity and remarkable redox capability<sup>5</sup> and hence is widely used as a heterogeneous catalyst<sup>6</sup> and oxygen storage component<sup>4</sup>. Because the key element is the oxygen vacancy<sup>7</sup>, the creation of oxygen vacancies is a prerequisite for such  $\text{CeO}_2$ -based ionic materials and devices.  $\text{CeO}_2$  has a fluorite-type structure with a coordination number of 8 for Ce to O atoms<sup>8</sup>, so aliovalent chemical doping (e.g., yttrium, samarium, and gadolinium) into  $\text{CeO}_2$  is one of the conventional approaches<sup>9</sup> to create oxygen vacancies. Nanoscaling, interfacing, and straining thin films are also known mechanisms to create oxygen vacancies<sup>10–12</sup>. However, the implementation of these approaches for practical applications requires further advancements because the fundamental understanding of oxygen vacancy formation at the atomic level is still lacking.

It was proposed that a space charge region (SCR)<sup>12–14</sup> could be formed by interfacing the fluorite  $\text{CeO}_2$  (space group  $Fm\bar{3}m$ ,  $a = 5.412 \text{ \AA}$ ) with a bixbyite oxide, such as  $\text{Y}_2\text{O}_3$  (space group  $Ia\bar{3}$ ,  $a = 10.607 \text{ \AA}$ ), along the  $[100]$  direction<sup>15,16</sup>. The bixbyite structure has a “pseudofluorite” structure with an ordered array of vacant oxygen sites occurring on every fourth site (Supplementary Fig. 1), providing an ideal atomic arrangement for forming an interfacial charge layer that originates from the valence mismatch between  $\text{Ce}(4+)$  and  $\text{Y}(3+)$ . However, the formation of an atomically well-defined (001) interface between the two binary oxides is energetically unfavorable, as the (001) surface has the highest surface energy among the low-index surfaces for both materials. In contrast, the (111) surfaces of fluorite and bixbyite structures are energetically more favorable because of their low surface energy<sup>17,18</sup>. Thus, determining the viability of the artificial creation of oxygen vacancies at an atomically well-defined (111) interface and understanding the (111) fluorite–bixbyite interface could open a new avenue toward the development of high-performance oxide-based ionotronic devices. Moreover, the  $\text{Ce}^{4+}\text{O}_2/\text{Y}^{3+}_2\text{O}_3$  interface offers an interfacial condition similar to that of semiconductor and perovskite-oxide heterointerfaces having polar discontinuity<sup>19–21</sup>. Therefore, understanding the details of the interfacial oxygen vacancy formation reported herein will provide useful insights into developing a novel concept of two-dimensional (2D) ionic channels using atomically engineered oxide interfaces.

In this work, we investigate the viability of colossal formation of oxygen vacancies in  $\text{CeO}_2/\text{Y}_2\text{O}_3$  superlattices with atomically well-defined (111) interfaces formed within a nanobrush architecture (Fig. 1). The nanobrush superlattices offer many advantages over 2D thin films, including much larger surface areas and a larger number of interfaces than exist in planar films, which are useful for many applications in various technologically relevant areas<sup>22</sup>.

## Results

### Precision synthesis of a (111) fluorite–bixbyite nanobrush.

Figure 1a shows a cross-sectional high-angle annular dark-field (HAADF) image obtained using scanning transmission electron microscopy (STEM) from a  $1.4\text{-}\mu\text{m}$ -thick  $\text{CeO}_2/\text{Y}_2\text{O}_3$  nanobrush superlattice grown on a  $\text{Y}_2\text{O}_3$ -stabilized  $\text{ZrO}_2$  (YSZ)-buffered (001) silicon substrate. The Z-contrast (Z denotes the atomic number) HAADF image clearly reveals alternating stacks of  $\text{CeO}_2$  ( $Z_{\text{Ce}} = 58$ ) and  $\text{Y}_2\text{O}_3$  ( $Z_{\text{Y}} = 39$ ) layers. The  $[(\text{CeO}_2)_6 \text{ u.c.}/(\text{Y}_2\text{O}_3)_2 \text{ u.c.}]_{200}$  nanobrush superlattice was grown by pulsed laser deposition under

an extremely nonequilibrium supersaturated condition, which is far away from the conventional condition optimized for the layer-by-layer growth of 2D thin films. Despite the porous architecture with single-crystalline bristles and the large thickness, the created nanostructure was highly epitaxial and (001)-oriented, as confirmed by X-ray diffraction (XRD)  $2\theta$ – $\theta$  scans and pole figure measurements (Supplementary Fig. 2). Based upon the XRD data, the epitaxial orientation relationship of the  $\text{CeO}_2/\text{Y}_2\text{O}_3$  nanobrush superlattice on the YSZ-buffered (001) silicon substrate was  $\text{Y}_2\text{O}_3(001)\parallel\text{CeO}_2(001)\parallel\text{YSZ}(001)\parallel\text{Si}(001)$ , a finding also confirmed by selected area electron diffraction (Supplementary Fig. 3). While a variety of oxide nanostructures—such as nanorods<sup>23,24</sup>, nanowires<sup>25</sup>, nanobelts<sup>26</sup>, and nanonails<sup>27</sup>—have been successfully demonstrated, our nanobrush architecture is a revolutionary new form of oxide nanostructure in which the growth is governed by both diffusion-limited aggregation and the shadow effect (Supplementary Fig. 4). The details of the growth mechanism for oxide nanobrush architectures were reported elsewhere<sup>28</sup>. Interestingly, a characteristic chevron pattern can be seen within each bristle. This chevron pattern originates from the  $\{111\}$  facet formation for both  $\text{CeO}_2$  and  $\text{Y}_2\text{O}_3$ , owing to the lowest surface energy<sup>17,18</sup>. The interface connection of the  $\{111\}$  facets of the  $\text{CeO}_2$  and  $\text{Y}_2\text{O}_3$  sublayers was the key to the spontaneous formation of oxygen vacancies on the  $\text{CeO}_2$  side, as discussed below.

We performed atom probe tomography (APT) on the  $\text{CeO}_2$ – $\text{Y}_2\text{O}_3$  nanobrush to reveal the three-dimensional (3D) geometry of the nanobristles. Owing to the small nanobristle size (only  $\sim 30 \text{ nm}$  in the lateral dimension), the growth of a nanobristle on a micron-wide silicon-tip for APT was highly challenging. Nevertheless, we successfully grew a nanobrush sample on a special silicon microtip array and prepared an APT specimen via focused ion beam (FIB) milling, as shown in Supplementary Fig. 5. Figure 1b shows an APT image (see also Supplementary Movie 1 for 3D view) of a  $(\text{CeO}_2)_6 \text{ u.c.}/(\text{Y}_2\text{O}_3)_2 \text{ u.c.}$  nanobristle. The APT investigation confirmed the chevron pattern on the nanobristles. The overall “Christmas tree-like” shape of the bristles and the chevron pattern on each bristle are only visible along the  $\langle 110 \rangle$  direction, whereas the  $\langle 100 \rangle$  directional view reveals a horizontal layer-by-layer stacking of superlattices, clearly visualizing the 3D geometry of the nanobrush samples.

Figure 1c schematically shows top and cross-sectional views of the oxygen coordination mismatch at the (111) interface between the fluorite and the bixbyite, depicting the underlying mechanism for the formation of oxygen vacancies. Only oxygen atoms are shown to reveal the difference in the oxygen network between (111) $\text{CeO}_2$  and (111) $\text{Y}_2\text{O}_3$ . While the structure of a (001) fluorite/bixbyite interface is rather simple (Supplementary Fig. 1), the oxygen network along the (111) plane is rather complex, forming a triangular network of oxygen vacant sites in  $\text{Y}_2\text{O}_3$ . The cross-sectional views cut along the C1, C2, and C3 directions clearly visualize the oxygen mismatch between the two materials. This interfacial oxygen coordination mismatch can explain the underlying mechanism behind the formation of the interfacial oxygen vacancies. To cope with the valence mismatch in  $\text{Y}^{3+}$  vs.  $\text{Ce}^{4+}$ , the following two scenarios were considered: (1) formation of an oxygen interstitial in  $\text{Y}_2\text{O}_3$  and (2) formation of an oxygen vacancy in  $\text{CeO}_2$ .

### Artificial formation of oxygen vacancies at the (111) interface.

To confirm the viability of highly confined formation of oxygen vacancies at a (111) interface in a  $\text{CeO}_2$ – $\text{Y}_2\text{O}_3$  nanobrush, we performed a systematic STEM study. Figure 2 shows HAADF and low-angle annular dark-field (LAADF) images obtained from both the tip and middle parts of a  $[(\text{CeO}_2)_6 \text{ u.c.}/(\text{Y}_2\text{O}_3)_2 \text{ u.c.}]$

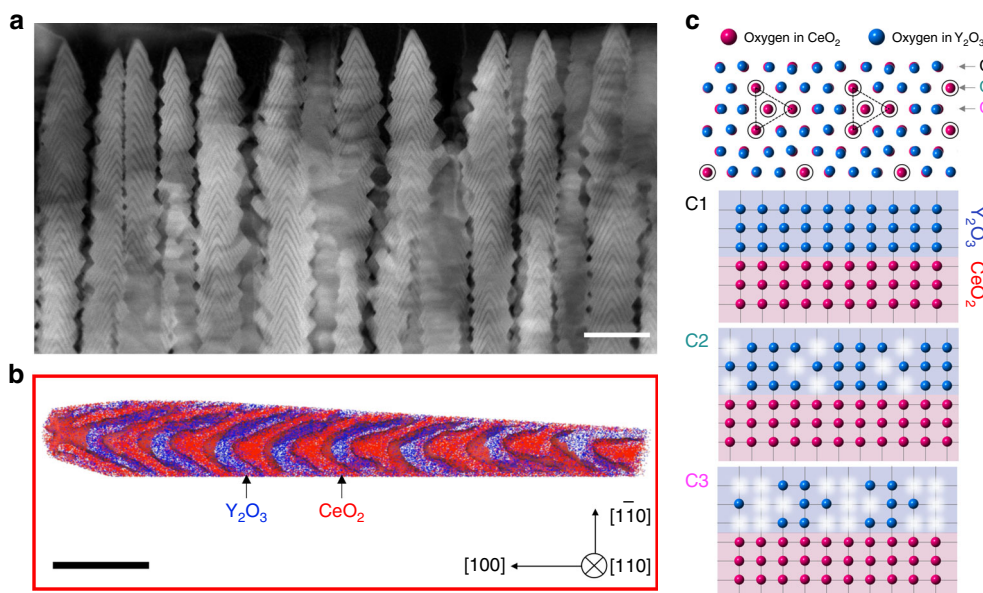


**Fig. 1**  $\text{CeO}_2/\text{Y}_2\text{O}_3$  nanobrush and the atomic configurations of the (111) interface. **a** A cross-sectional HAADF-STEM image of a  $[(\text{CeO}_2)_6 \text{ u.c.}/(\text{Y}_2\text{O}_3)_2 \text{ u.c.}]_{200}$  nanobrush superlattice with a thickness of  $1.4 \mu\text{m}$  grown on a (001) YSZ-buffered silicon substrate, taken along the [110] direction. Because of the nonuniform thickness of sublayers originating from faceting, we use the average thickness of the individual layers. Note that oxide nanostructures were grown on (001) YSZ-buffered silicon substrates, as TEM imaging for samples grown directly on YSZ was difficult because of severe charging of electrons. The scale bar corresponds to  $50 \text{ nm}$ . **b** Atom probe tomography (APT) reconstruction with Ce and Y atoms displayed as red and blue points, respectively, showing a three-dimensional view of the free-standing  $[(\text{CeO}_2)_6 \text{ u.c.}/(\text{Y}_2\text{O}_3)_2 \text{ u.c.}]_{200}$  internal structure. The scale bar corresponds to  $20 \text{ nm}$ . **c** Schematic of a (111) interface between  $\text{CeO}_2$  (fluorite) and  $\text{Y}_2\text{O}_3$  (bixbyite), in which red and blue circles represent oxygen atoms in  $\text{CeO}_2$  and  $\text{Y}_2\text{O}_3$ , respectively. Cations are not shown. The (111)  $\text{Y}_2\text{O}_3/\text{CeO}_2$  interface is a combination of three different anion arrays, C1, C2, and C3. A cross-section of the C1 array shows a perfect match between numbers of oxygen atoms on interfacing  $\text{CeO}_2$  and  $\text{Y}_2\text{O}_3$  sides. In contrast, on the  $\text{Y}_2\text{O}_3$  side of the interface, a cross-section shows on average one oxygen vacancy every four sites in the C2 array and one oxygen vacancy every two sites in the C3 array.

nanobristle. In the HAADF images (Fig. 2a, b), the chevron pattern of a stack of alternating  $\text{CeO}_2$  and  $\text{Y}_2\text{O}_3$  layers is clearly visible. As indicated in Fig. 2e, the angle between the two {111} facets is  $\sim 70.5^\circ$ , which can readily be seen when viewed along the [110] direction, confirming the formation of (111) interfaces. The STEM images also reveal that the outer portion of each layer is thinner than its center part. In addition, a fast Fourier transform analysis clearly shows a fully coherent interface (i.e., free from any dislocations) formed between  $\text{CeO}_2$  and  $\text{Y}_2\text{O}_3$  layers (Supplementary Fig. 6). Moreover, at the edge region of the bristles in the HAADF images, the  $\text{CeO}_2$  layers encase the  $\text{Y}_2\text{O}_3$  layers. The capping yields vertically connected  $\text{CeO}_2$  (Supplementary Fig. 7). This may be attributed to the lower Ehrlich-Schwoebel barrier<sup>29</sup> for  $\text{CeO}_2$  on  $\text{Y}_2\text{O}_3$  than for  $\text{Y}_2\text{O}_3$  on  $\text{CeO}_2$ .

The two interfacial reconstruction scenarios mentioned previously, i.e., (1) formation of an oxygen interstitial on the  $\text{Y}_2\text{O}_3$  side and (2) formation of an oxygen vacancy and subsequent  $\text{Ce}^{3+}$  ions on the  $\text{CeO}_2$  side, can result in a local lattice distortion. Such structural disorder can be detected by LAADF imaging, as it leads to electron dechanneling of the incident e-beam<sup>30,31</sup>. As shown in Fig. 2c, d, the LAADF images reveal an enhanced intensity at the interface between  $\text{CeO}_2$  and  $\text{Y}_2\text{O}_3$ . Through a careful examination of the images, we found that the bright contrast originated from the  $\text{CeO}_2$  side of the interfaces (see the yellow lines in Fig. 2a–d). Note that we have not observed any bixbyite  $\text{Ce}_2\text{O}_3$  structures at the  $\text{CeO}_2/\text{Y}_2\text{O}_3$  interface, as confirmed by HAADF imaging (Supplementary Fig. 8). Considering the fact that the lattice mismatch between  $\text{Ce}_2\text{O}_3$  and  $\text{Y}_2\text{O}_3$  is  $\sim 10\%$ , the formation of the bixbyite  $\text{Ce}_2\text{O}_3$  phase may not be energetically favorable at the interfaces. LAADF imaging also confirmed that the structurally distorted layer owing to the chemical expansion spanned over  $\sim 1 \text{ nm}$  in thickness (Supplementary Fig. 9). In addition, a previous TEM study reported a

large lattice expansion occurred in  $\text{CeO}_2$  nanoparticles, owing to the formation of oxygen vacancies with  $\text{Ce}^{3+}$  ions, without changing the original fluorite structure<sup>32</sup>. Thus, our results suggest that the highly localized formation of a large number of oxygen vacancies on the  $\text{CeO}_2$  side of the interfaces was responsible for the observed electron dechanneling. The formation of interfacial oxygen vacancies was further confirmed by a geometric phase analysis (GPA) of STEM images. As shown in Fig. 2f, the GPA result reveals a significant lattice expansion by up to  $3\%$  for the  $\text{CeO}_2$  interfacial regions, consistent with the LAADF results. Furthermore, we can also exclude the possibility of the formation of oxygen interstitials on the  $\text{Y}_2\text{O}_3$  side of the interface—one of the two interfacial reconstruction scenarios mentioned earlier based upon the STEM data—as we have not observed any atomic structural changes in  $\text{Y}_2\text{O}_3$  interfacial layers.

**Interfacial cerium valence modulation.** The interfacial oxygen vacancy formation was further investigated by electron energy-loss spectroscopy (EELS), which highlighted the elemental distributions, atomic configurations, and bonding states of both Ce and O. Figure 3a shows an elemental map produced using the  $\text{Ce-}M_{4,5}$  edge in the vicinity of the (111) $\text{CeO}_2$ /(111) $\text{Y}_2\text{O}_3$  interface, revealing interfaces that are not only structurally well-defined but also chemically sharp. Background-subtracted  $\text{Ce-}M_{4,5}$  edge spectra obtained from each atomic plane across the (111) $\text{CeO}_2$ /(111) $\text{Y}_2\text{O}_3$  interface are shown in Fig. 3b. The peak positions of  $\text{Ce-}M_{4,5}$  edges are shifted to a lower energy-loss region for the reduced  $\text{CeO}_2$  interfacial layers, as compared with that of the  $\text{CeO}_2$  interior layer. The  $\text{Ce-}M_{4,5}$  edges originate from transitions between the  $3d$  and  $4f$  states ( $M_4$  corresponds to the  $3d_{3/2}$  to  $4f_{5/2}$  transition and  $M_5$  corresponds to the  $3d_{5/2}$  to  $4f_{7/2}$  transition) combined with ligand hole effects and valence-sensitive fine structures. Thus, spatially resolved chemical information<sup>33,34</sup> was



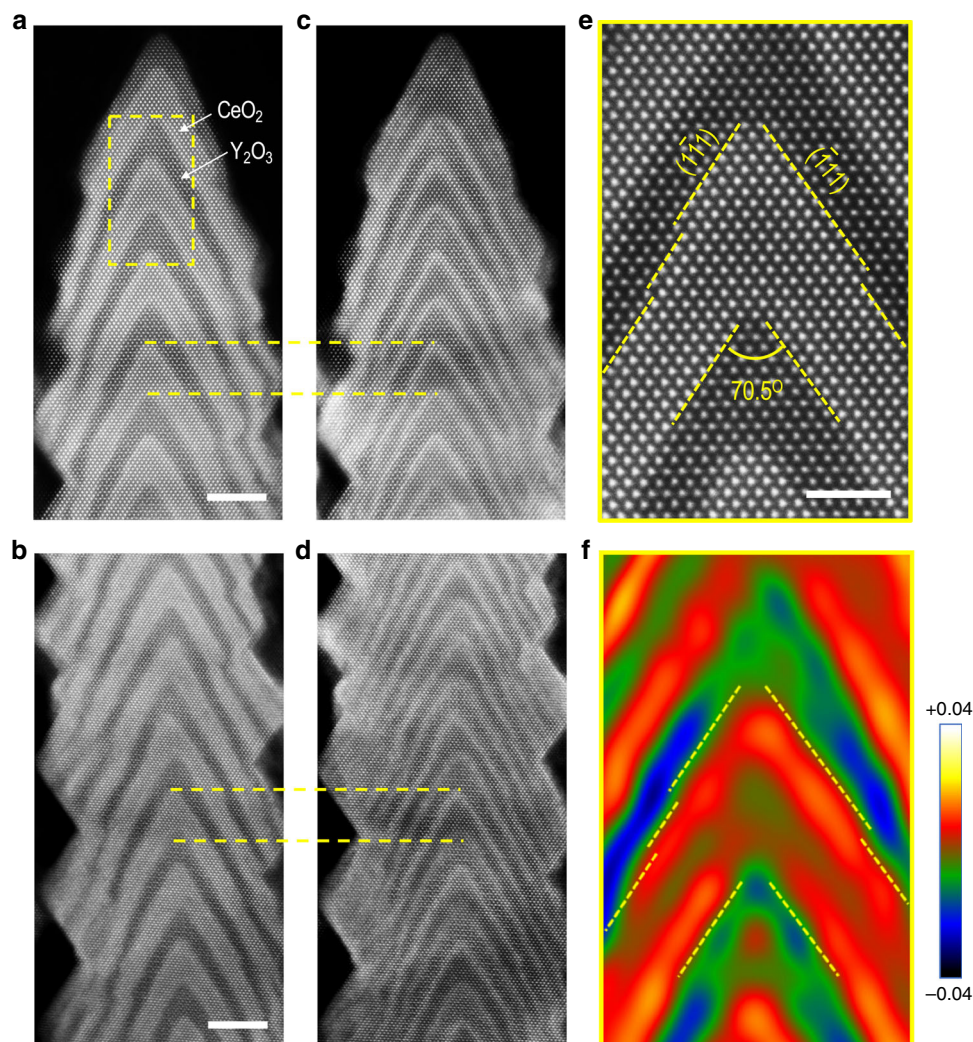


**Fig. 2** (111) interface and local strain in a free-standing  $\text{CeO}_2/\text{Y}_2\text{O}_3$  nanobristle. **a, b** HAADF images and **c, d** their corresponding LAADF images taken from the top and middle regions of a free-standing  $\text{CeO}_2/\text{Y}_2\text{O}_3$  nanobristle along the [110] direction. As indicated by the yellow dashed lines, the brighter contrast at the outer parts of the  $\text{CeO}_2$  sublayers in the LAADF images suggests locally enhanced lattice distortions due to the formation of oxygen vacancies. The scale bar corresponds to 5 nm. **e** Magnified HAADF image showing atomically abrupt interfaces and {111} Ce facets between  $\text{CeO}_2$  and  $\text{Y}_2\text{O}_3$  layers. The scale bar corresponds to 2 nm. **f** Geometric phase analysis of the HAADF image shown in **e** reveals a lattice expansion of the outer parts of the  $\text{CeO}_2$  layers.

obtained from EELS measurements. Using linear combinations of  $\text{Ce}-M_{4,5}$  reference spectra from  $\text{CeO}_2$  and  $\text{Ce}_2\text{O}_3$ <sup>34</sup>, the valence states of the reduced cerium atoms near the interface were roughly estimated to be  $\text{Ce}^{+3.3}$  (the nearest to the interface) and  $\text{Ce}^{+3.6}$  (the second nearest), which correspond to  $\text{CeO}_{1.65}$  and  $\text{CeO}_{1.8}$ , respectively, as illustrated in Fig. 3c. These oxidation states led to 17.5% and 10% of missing oxygen atoms, respectively, which was indeed a large amount, especially considering the robust interface lattice structures observed by STEM. Background-subtracted O-K spectra averaged along the (111)O planes show a considerable number of oxygen vacancies are formed at interfaces to cope with the interfacial charge mismatch (Supplementary Fig. 10). It is worth stressing that such an interfacial charge modulation is a powerful method of creating a high concentration of oxygen vacancies. Interestingly, our STEM and EELS results suggest that the formation of oxygen vacancies at the (111) interface between the fluorite and the bixbyite is not attributable to the creation of SCRs in the  $\text{CeO}_2$  layer, in which the calculated Debye length ( $\lambda$ ) of  $\sim 2.4$  nm at 300 K<sup>16,35</sup> can result in a  $\sim 10$  nm thick regime of overlapping space charges ( $4\lambda$ )<sup>12</sup>.

#### Spatial distributions of oxygen defects at the (111) interface.

To clarify the role of the (111) interface in creating the oxygen vacancies, the defect formation energy of a neutral oxygen vacancy complex,  $(\text{Ce}'_{\text{Ce}} - \text{V}_{\text{O}} - \text{Ce}'_{\text{Ce}})^{\times}$ , at the (111) interface was computed by density functional theory (DFT) calculations (Supplementary Fig. 11). The DFT calculations indicated that the positive charge of oxygen vacancies was always compensated by two  $\text{Ce}^{3+}$  ions (Supplementary Fig. 12). In addition, the DFT results revealed that the formation energies of oxygen vacancies and  $\text{Ce}^{3+}$  ions at the heterointerface were  $\sim 1.8$  and  $\sim 0.5$  eV, respectively. These values are lower than those in bulk  $\text{CeO}_2$  as a result of the lower electronic state of the polaron (i.e., reduced cerium cations,  $\text{Ce}'_{\text{Ce}}$ ) and the easier local lattice relaxation at the interface. These low formation energies increased the number of both the oxygen vacancies and the  $\text{Ce}^{3+}$  ions at the interface, leading to the segregation of oxygen vacancies on the  $\text{CeO}_2$  side of the interface, as shown in Fig. 4. The calculation result showing up to 10% oxygen loss at the interface is quantitatively in good agreement with experimental observations of the EELS data shown in Fig. 3b, c. It is also worth noting that the vacancy

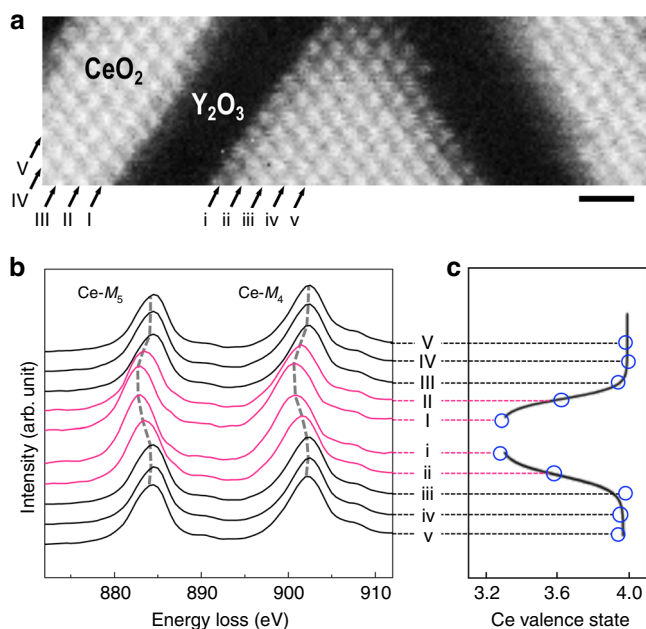


**Fig. 3 Interfacial valence changes seen by STEM/EELS.** **a** Atomic-resolution EELS map for the Ce- $M_{4,5}$  edges from a local area in a  $\text{CeO}_2$ - $\text{Y}_2\text{O}_3$  nanobristle, revealing an atomically abrupt (111) interface. The scale bar corresponds to 1 nm. **b** Ce- $M_{4,5}$  EELS spectra averaged along the (111)Ce atom planes. The dashed lines indicate the chemical shift of the Ce- $M_5$  and Ce- $M_4$  edges at the interface between  $\text{CeO}_2$  and  $\text{Y}_2\text{O}_3$  as indicated by the EELS spectra in red. The latter were taken from the two interfacial  $\text{CeO}_2$  layers interleaved by a  $\text{Y}_2\text{O}_3$  layer, indicating the presence of reduced  $\text{CeO}_2$  layers ( $\sim 2$  u.c. thick). **c** Average Ce valence states in the (111)Ce atom planes indicated in **b**, revealing the valence change in interfacial  $\text{CeO}_2$  layers.

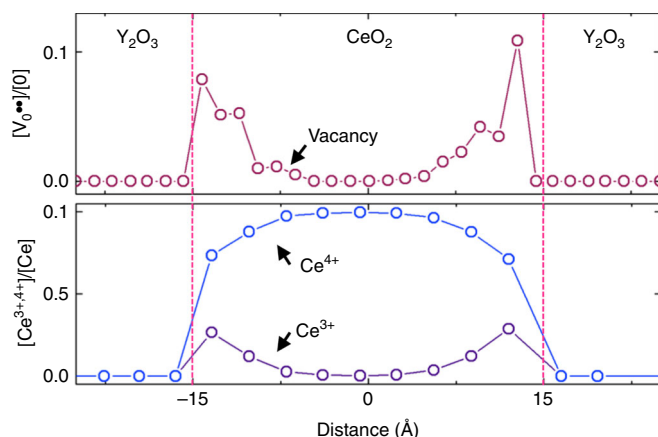


**Fig. 4 Cation and oxygen vacancy distributions at the (111)  $\text{CeO}_2/\text{Y}_2\text{O}_3$  interface.** Distribution profiles of oxygen vacancy (top) and  $\text{Ce}^{3+}$ ,  $\text{Ce}^{4+}$  (bottom) equilibrated at 700 °C in  $\text{CeO}_2$  and  $\text{Y}_2\text{O}_3$  calculated by hybrid Monte Carlo (MC) and molecular dynamics (MD) simulations. The interfaces enrich  $\text{Ce}^{3+}$  and oxygen vacancies simultaneously within  $\text{CeO}_2$ . The concentration of oxygen vacancies can reach up to 10% at the interface, spanning over  $\sim 1$  nm.

segregation was not driven solely by an electrostatic potential at the interface, as the (111) surface was nonpolar so that an SCR could not easily form, and the defect concentration in ceria was high enough to screen out any electrostatic potential (Supplementary Fig. 13). Therefore, the (111) fluorite-bixbyite interface could induce a larger number of oxygen vacancies without the

creation of an SCR, which differs from the mechanism proposed for (001) interfaces of fluorite-bixbyite systems in previous studies<sup>15,16</sup>. As was confirmed by STEM imaging, classical force field (FF) simulation also confirmed that the  $\text{CeO}_2$  side of the interfaces always remained as the fluorite structure, even though the interface had a high concentration of oxygen vacancies (Supplementary Fig. 14).

## Discussion

There have been several studies of creating oxygen defects, understanding the underlying mechanism for their formation, and probing their existence in mixed ionic and electronic conducting materials<sup>13,14</sup>. However, identifying a new means to artificially create and control highly confined interfacial oxygen vacancies has been a huge challenge. The present work elucidates that interfaces between the fluorite  $\text{CeO}_2$  and the bixbyite  $\text{Y}_2\text{O}_3$  can provide an excellent platform for developing new ionic materials. Creating atomically sharp (111) fluorite/bixbyite interfaces in the nanobrush architecture provides a completely new approach to spontaneously creating oxygen vacancies through interfacial charge modulation. In contrast to the well-known SCR effect, the (111) fluorite/bixbyite interface creates and confines oxygen vacancies within two to three atomic layers on the  $\text{CeO}_2$  side of the (111) interface. It is remarkable that a large number of oxygen vacancies can be accommodated by taking advantage of the novel interface architecture while leaving the lattice structure intact.

We further demonstrated a new “synthesis science” approach<sup>36</sup> to making a specific interfacial nanomaterial with a vertically aligned geometry and a largely increased area of the (111)-oriented surface. As shown in Fig. 1a, our  $\text{CeO}_2$ - $\text{Y}_2\text{O}_3$  nanobrush has a highly porous topography. Therefore, the quantitative information on porosity was important for accurately determining the surface area, which was an extremely challenging task. The difficulty was overcome by using small-angle neutron scattering (SANS), as shown in Supplementary Fig. 15. The SANS results revealed that the upper limit of the porosity was  $\sim 49\%$ . More details on the SANS measurement and data analysis can be found elsewhere<sup>28</sup>. The high porosity is highly advantageous for many technical applications, in which a large contact area can improve (electro-)chemical activity, e.g., electrodes of solid oxide fuel/electrolysis cells<sup>37</sup>, oxygen permeation membranes<sup>38</sup>, chemical sensors<sup>39</sup>, and catalysts<sup>40</sup>. In our study, the SANS data confirmed that the  $\sim 1.4$ - $\mu\text{m}$ -thick nanobrushes had a surface area that is over 200 times greater than that of a 2D thin film. Therefore, these advances are major technical accomplishments that provide a new means to develop high-performance energy conversion devices, novel catalysts, nonvolatile memories, and memristive computing devices.

## Methods

**Synthesis of nanobrush samples.** Micron-thick single-crystalline fluorite-bixbyite ( $\text{CeO}_2$ - $\text{Y}_2\text{O}_3$ ) nanobrush superlattices were fabricated using pulsed laser epitaxy (KrF,  $\lambda = 248$  nm) with sintered  $\text{CeO}_2$  and  $\text{Y}_2\text{O}_3$  targets. While all of the samples studied were grown on single-crystal (001) YSZ substrates, the samples for STEM and APT were grown on YSZ-buffered (001) silicon substrates without deteriorating the sample quality to avoid the charging effect resulting from the highly insulating YSZ substrate. Details on the growth of a YSZ buffer layer and the epitaxial relationship of YSZ and silicon can be found elsewhere<sup>41–44</sup>. All of the samples were deposited at 700 °C at an oxygen partial pressure of 100 mTorr. The sample structure and crystallinity were characterized by high-resolution four-circle XRD.

**Scanning transmission electron microscopy.** Cross-sectional TEM specimens were prepared using ion milling after mechanical thinning and precision polishing. HAADF and LAADF imaging and EELS analysis were carried out in a scanning transmission electron microscope (Nion UltraSTEM100) operated at 100 keV. The microscope is equipped with a cold field-emission gun and an aberration corrector



for sub-Ångström resolution. Inner detector angles of 78 and 30 mrad were used for HAADF and LAADF imaging, respectively. The convergence semiangle for the electron probe was set to 30 mrad.

**Atom probe tomography.** APT specimens were prepared by first coating a silicon microtip array with the  $\text{CeO}_2/\text{Y}_2\text{O}_3$  nanobristles. An FEI Nova 200 dual-beam scanning electron microscope/FIB was used to fabricate APT needles from the nanobristles grown on the silicon microtip array. A 300 nm platinum layer was deposited by FIB, followed by several annular milling steps and a final 2 kV mill to fabricate needle-shaped specimens ready for APT analysis. After sample preparation, the specimen was loaded into the LEAP 4000XR and analyzed using laser mode with a 10 ps/100 pJ laser pulse, a 50 K base temperature, a 125 kHz pulse repetition rate, and a detection rate of 1 ion per 500 pulses. Reconstruction and analysis were performed using the CAMECA integrated visualization and analysis software package.

**Density functional theory calculations.** In this work, the DFT calculations were performed with VASP<sup>45–47</sup> using the projector augmented wave method. Generalized gradient approximation with the PBE exchange correlation functional<sup>48</sup> and an energy cutoff of 500 eV were used. To properly simulate  $\text{Ce}^{3+}$ , a Hubbard U correction<sup>49</sup> was applied to the Ce 4f orbital with  $U = 5$  eV. The model of the  $\text{CeO}_2/\text{Y}_2\text{O}_3$  {111} interface was constructed according to the TEM observation, in which  $\text{Y}_2\text{O}_3$  was stretched biaxially by 1.4% and  $\text{CeO}_2$  was compressed by 1.4%. The interface model consisted of 24  $\text{Y}_2\text{O}_3$  and 48  $\text{CeO}_2$ . The simulation cell was hexagonal with  $a = 1.535$  nm,  $c = 1.880$  nm, and  $\gamma = 120^\circ$ . Both the  $\text{CeO}_2$  layer and the  $\text{Y}_2\text{O}_3$  layer were 0.94 nm thick. For all calculations, a  $k$ -point mesh of  $2 \times 2 \times 1$  was used. The vacancy formation energy was computed by removing a neutral oxygen atom close to the interface or in the middle of the  $\text{CeO}_2$  layer.

**Hybrid Monte Carlo and molecular dynamics with classical force field.** The vacancy and  $\text{Ce}^{3+}$  concentration profiles were computed with a hybrid MC and MD algorithm using a classical FF. The simulation technique is well documented in the original paper<sup>50</sup> and our previous work<sup>51</sup>. The simulation was started with a uniform distribution of  $\text{Ce}^{3+}$  and oxygen vacancies in the  $\text{CeO}_2$  layer. In the MC simulation, only  $\text{Ce}^{3+}$  and  $\text{Ce}^{4+}$  ions were allowed to swap their positions, whereas in the MD simulation, the oxygen vacancies could diffuse to either  $\text{Y}_2\text{O}_3$  or  $\text{CeO}_2$  layers. More than  $10^5$  MC trials and 6 ns MD simulations at 600 °C were performed. The defect concentration profiles were obtained by averaging the last 5000 configurations of each single calculation.

**Small-angle neutron scattering.** Room-temperature SANS measurements were performed using EQ-SANS at the Spallation Neutron Source at Oak Ridge National Laboratory<sup>52,53</sup>. Data were collected in 60 Hz mode with a  $Q$ -range between  $\sim 0.015$  and  $0.35 \text{ \AA}^{-1}$ . The 2D scattering data were reduced using the MantidPlot software according to standard procedures<sup>54</sup>. The SANS signals from  $\text{CeO}_2\text{-Y}_2\text{O}_3$  nanobrush samples were subtracted the background scattering from a YSZ bare substrate.

## Data availability

Data supporting the findings of this study are available from the corresponding author upon reasonable request.

## Code availability

The VASP code, which is available for purchase, was used for the calculations in this paper. The configuration files used in these calculations are all available upon request from the authors.

Received: 26 August 2019; Accepted: 16 February 2020;

Published online: 13 March 2020

## References

- Chueh, W. C. & Haile, S. M. Electrochemistry of mixed oxygen ion and electron conducting electrodes in solid electrolyte cells. *Annu. Rev. Chem. Biomol. Eng.* **3**, 313–341 (2012).
- Wang, G. et al. Hydrogen-treated  $\text{TiO}_2$  nanowire arrays for photoelectrochemical water splitting. *Nano Lett.* **11**, 3026–3033 (2011).
- Barsan, N., Koziej, D. & Weimar, U. Metal oxide-based gas sensor research: How to? *Sens. Actuators B* **121**, 18–35 (2007).
- Yao, H. C. & Yao, Y. F. Y. Ceria in automotive exhaust catalysts: I. Oxygen storage. *J. Catal.* **86**, 254–265 (1984).
- Skorodumova, N. V., Simak, S. I., Lundqvist, B. I., Abrikosov, I. A. & Johansson, B. Quantum origin of the oxygen storage capability of ceria. *Phys. Rev. Lett.* **89**, 166601 (2002).
- Trovarelli, A. Catalytic properties of ceria and  $\text{CeO}_2$ -containing materials. *Catal. Rev.* **38**, 439–520 (1996).
- Esch, F. et al. Electron localization determines defect formation on ceria substrates. *Science* **309**, 752–755 (2005).
- Wu, L. et al. Oxidation state and lattice expansion of  $\text{CeO}_{2-x}$  nanoparticles as a function of particle size. *Phys. Rev. B* **69**, 125415 (2004).
- Balazs, G. B. & Glass, R. S. AC-impedance studies of rare-earth-oxide doped ceria. *Solid State Ion.* **76**, 155–162 (1995).
- Kim, S., Fleig, J. & Maier, J. Space charge conduction: simple analytical solutions for ionic and mixed conductors and application to nanocrystalline ceria. *Phys. Chem. Chem. Phys.* **5**, 2268–2273 (2003).
- Balaji Gopal, C. et al. Equilibrium oxygen storage capacity of ultrathin  $\text{CeO}_{2-\delta}$  depends non-monotonically on large biaxial strain. *Nat. Commun.* **8**, 15360 (2017).
- Sata, N., Eberman, K., Eberl, K. & Maier, J. Mesoscopic fast ion conduction in nanometre-scale planar heterostructures. *Nature* **408**, 946–949 (2000).
- Guo, X. & Maier, J. Comprehensive modeling of ion conduction of nanosized  $\text{CaF}_2/\text{BaF}_2$  multilayer heterostructures. *Adv. Funct. Mater.* **19**, 96–101 (2009).
- Maier, J. Ionic conduction in space charge regions. *Prog. Solid State Chem.* **23**, 171–263 (1995).
- Shen, W. D., Jiang, J. & Hertz, J. L. Beneficial lattice strain in heterogeneously doped ceria. *J. Phys. Chem. C* **118**, 22904–22912 (2014).
- Shen, W. D. et al. Two-dimensional vacancy trapping in yttria doped ceria. *Solid State Ion.* **255**, 13–20 (2014).
- Walsh, A. & Catlow, C. R. A. Structure, stability and work functions of the low index surfaces of pure indium oxide and Sn-doped indium oxide (ITO) from density functional theory. *J. Mater. Chem.* **20**, 10438–10444 (2010).
- Yang, Z., Woo, T. K., Baudin, M. & Hermansson, K. Atomic and electronic structure of unreduced and reduced  $\text{CeO}_2$  surfaces: A first-principles study. *J. Chem. Phys.* **120**, 7741–7749 (2004).
- Baraff, G. A., Appelbaum, J. A. & Hamann, D. R. Self-consistent calculation of the electronic structure at an abrupt GaAs-Ge interface. *Phys. Rev. Lett.* **38**, 237–240 (1977).
- Harrison, W. A., Kraut, E. A., Waldrop, J. R. & Grant, R. W. Polar heterojunction interfaces. *Phys. Rev. B* **18**, 4402–4410 (1978).
- Ohtomo, A., Muller, D. A., Grazul, J. L. & Hwang, H. Y. Artificial charge-modulation in atomic-scale perovskite titanate superlattices. *Nature* **419**, 378–380 (2002).
- Pollock, T. M., Lipkin, D. M. & Hemker, K. J. Multifunctional coating interlayers for thermal-barrier systems. *MRS Bull.* **37**, 923–931 (2012).
- Lu, X. et al. Facile synthesis of large-area manganese oxide nanorod arrays as a high-performance electrochemical supercapacitor. *Energy Environ. Sci.* **4**, 2915–2921 (2011).
- Jiang, J., Henry, L. L., Gnanasekar, K. I., Chen, C. & Meletis, E. I. Self-assembly of highly epitaxial (La,Sr) $\text{MnO}_3$  nanorods on (001)  $\text{LaAlO}_3$ . *Nano Lett.* **4**, 741–745 (2004).
- Wang, Z. L. & Song, J. Piezoelectric nanogenerators based on zinc oxide nanowire arrays. *Science* **312**, 242–246 (2006).
- Kong, X. Y. & Wang, Z. L. Spontaneous polarization-induced nanohelices, nanosprings, and nanorings of piezoelectric nanobelts. *Nano Lett.* **3**, 1625–1631 (2003).
- Lao, J. Y., Huang, J. Y., Wang, D. Z. & Ren, Z. F. Hierarchical oxide nanostructures. *J. Mater. Chem.* **14**, 770–773 (2004).
- Lee, D. et al. Nonequilibrium synthesis of highly porous single-crystalline oxide nanostructures. *Adv. Mater. Interfaces* **4**, 1601034 (2017).
- Pierre-Louis, O., D'Orsogna, M. R. & Einstein, T. L. Edge diffusion during growth: The kink Ehrlich-schwoebel effect and resulting instabilities. *Phys. Rev. Lett.* **82**, 3661–3664 (1999).
- Cowley, J. M. & Huang, Y. Dechanneling contrast in annular dark-field STEM. *Ultramicroscopy* **40**, 171–180 (1992).
- Muller, D. A., Nakagawa, N., Ohtomo, A., Grazul, J. L. & Hwang, H. Y. Atomic-scale imaging of nanoengineered oxygen vacancy profiles in  $\text{SrTiO}_3$ . *Nature* **430**, 657–661 (2004).
- Hailstone, R. K., DiFrancesco, A. G., Leong, J. G., Allston, T. D. & Reed, K. J. A study of lattice expansion in  $\text{CeO}_2$  nanoparticles by transmission electron microscopy. *J. Phys. Chem. C* **113**, 15155–15159 (2009).
- Karnatak, R. et al. X-ray absorption studies of  $\text{CeO}_2$ ,  $\text{PrO}_2$ , and  $\text{TbO}_2$ . I. Manifestation of localized and extended f states in the 3d absorption spectra. *Phys. Rev. B* **36**, 1745 (1987).
- Garvie, L. & Buseck, P. Determination of  $\text{Ce}^{4+}/\text{Ce}^{3+}$  in electron-beam-damaged  $\text{CeO}_2$  by electron energy-loss spectroscopy. *J. Phys. Chem. Solids* **60**, 1943–1947 (1999).
- Hwang, J. H. & Mason, T. O. Defect chemistry and transport properties of nanocrystalline cerium oxide. *Z. Phys. Chem.* **207**, 21–38 (1998).
- U.S. Department of Energy, Office of Science. *Report of the Basic Energy Sciences Workshop on Basic Research Needs for Synthesis Science for Energy Relevant Technology* (U.S. Department of Energy, Office of Science, 2016).

37. Chueh, W. C., Hao, Y., Jung, W. & Haile, S. M. High electrochemical activity of the oxide phase in model ceria–Pt and ceria–Ni composite anodes. *Nat. Mater.* **11**, 155–161 (2012).
38. Liu, S., Tan, X., Shao, Z. & Diniz da Costa, J. C. Ba<sub>0.5</sub>Sr<sub>0.5</sub>Co<sub>0.8</sub>Fe<sub>0.2</sub>O<sub>3-δ</sub> ceramic hollow-fiber membranes for oxygen permeation. *AIChE J.* **52**, 3452–3461 (2006).
39. Huang, X. J. & Choi, Y. K. Chemical sensors based on nanostructured materials. *Sens. Actuators B* **122**, 659–671 (2007).
40. Xie, X., Li, Y., Liu, Z.-Q., Haruta, M. & Shen, W. Low-temperature oxidation of CO catalysed by Co<sub>3</sub>O<sub>4</sub> nanorods. *Nature* **458**, 746–749 (2009).
41. Bayati, M. R., Joshi, S., Molaei, R., Narayan, R. J. & Narayan, J. Ultrafast switching in wetting properties of TiO<sub>2</sub>/YSZ/Si(001) epitaxial heterostructures induced by laser irradiation. *J. Appl. Phys.* **113**, 063706 (2013).
42. Chopra, A., Alexe, M. & Hesse, D. Fabrication and orientation control of highly cation-ordered epitaxial PbSc<sub>0.5</sub>Ta<sub>0.5</sub>O<sub>3</sub> thin films on Si (100). *J. Appl. Phys.* **117**, 044102 (2015).
43. Lee, H. N. et al. Epitaxial growth of non-c-oriented ferroelectric SrBi<sub>2</sub>Ta<sub>2</sub>O<sub>9</sub> thin films on Si(100) substrates. *Appl. Phys. A* **71**, 101–104 (2000).
44. Matthée, T. et al. Orientation relationships of epitaxial oxide buffer layers on silicon (100) for high-temperature superconducting YBa<sub>2</sub>Cu<sub>3</sub>O<sub>7-x</sub> films. *Appl. Phys. Lett.* **61**, 1240–1242 (1992).
45. Kresse, G. & Hafner, J. Ab initio molecular-dynamics simulation of the liquid-metal–amorphous-semiconductor transition in germanium. *Phys. Rev. B* **49**, 14251–14269 (1994).
46. Kresse, G. & Hafner, J. Ab initio molecular dynamics for liquid metals. *Phys. Rev. B* **47**, 558–561 (1993).
47. Kresse, G. & Joubert, D. From ultrasoft pseudopotentials to the projector augmented-wave method. *Phys. Rev. B* **59**, 1758–1775 (1999).
48. Perdew, J. P., Burke, K. & Ernzerhof, M. Generalized gradient approximation made simple. *Phys. Rev. Lett.* **77**, 3865–3868 (1996).
49. Dudarev, S. L. et al. Electronic structure and elastic properties of strongly correlated metal oxides from first principles: LSDA + U, SIC-LSDA and EELS study of UO<sub>2</sub> and NiO. *Phys. Status Solidi A* **166**, 429–443 (1998).
50. Lee, H. B., Prinz, F. B. & Cai, W. Atomistic simulations of grain boundary segregation in nanocrystalline yttria-stabilized zirconia and gadolinia-doped ceria solid oxide electrolytes. *Acta Mater.* **61**, 3872–3887 (2013).
51. Sun, L., Marrocchelli, D. & Yildiz, B. Edge dislocation slows down oxide ion diffusion in doped CeO<sub>2</sub> by segregation of charged defects. *Nat. Commun.* **6**, 6294 (2015).
52. Heller, W. T. et al. The suite of small-angle neutron scattering instruments at Oak Ridge National Laboratory. *J. Appl. Crystallogr.* **51**, 242–248 (2018).
53. Zhao, J. K., Gao, C. Y. & Liu, D. The extended Q-range small-angle neutron scattering diffractometer at the SNS. *J. Appl. Crystallogr.* **43**, 1068–1077 (2010).
54. Arnold, O. et al. Mantid-data analysis and visualization package for neutron scattering and  $\mu$  SR experiments. *Nucl. Instrum. Methods Phys. Res.* **764**, 156–166 (2014).

## Acknowledgements

The authors are grateful for helpful discussions with S.M. Haile, J. Maier, and H.L. Tuller. This work was supported by the US Department of Energy (DOE), Office of Science, Basic Energy Sciences, Materials Sciences and Engineering Division. A portion of this research used resources at the Center for Nanophase Materials Sciences

(STEM and APT) and the Spallation Neutron Source (SNS), which are U.S. DOE Office of Science User Facilities operated by Oak Ridge National Laboratory. Theoretical calculations used resources at the National Energy Research Scientific Computing Center, a U.S. DOE Office of Science User Facility operated under Contract No. DE-AC02-05CH11231. X-ray absorption fine structure work used resources of the Advanced Photon Source, a U.S. DOE Office of Science User Facility operated for the U.S. DOE Office of Science by Argonne National Laboratory under Contract No. DE-AC02-06CH11357.

## Author contributions

D.L. and X.G. contributed equally to this work. D.L. synthesized samples and performed basic characterizations with the help of L.F. X.G. performed STEM imaging and EELS data analysis with the help of M.F.C. L.S. performed DFT calculations and MC/MD simulations with help from Q.L. under the direction of B.Y. Y.J. and K.H. conducted initial sample analysis. J.P. conducted APT measurements. T.O.F., E.J.G., W.T.H., and M.R.F. performed EQ-SANS measurement and analysis. Y.C. and D.H. worked on XAFS measurements. H.N.L. initiated and coordinated the research. D.L., X.G., and H.N.L. wrote the manuscript with inputs from all authors.

## Competing interests

The authors declare no competing interests.

## Additional information

**Supplementary information** is available for this paper at <https://doi.org/10.1038/s41467-020-15153-8>.

**Correspondence** and requests for materials should be addressed to H.N.L.

**Peer review information** *Nature Communication* thanks the anonymous reviewers for their contributions to the peer review of this work.

**Reprints and permission information** is available at <http://www.nature.com/reprints>

**Publisher's note** Springer Nature remains neutral with regard to jurisdictional claims in published maps and institutional affiliations.



**Open Access** This article is licensed under a Creative Commons Attribution 4.0 International License, which permits use, sharing, adaptation, distribution and reproduction in any medium or format, as long as you give appropriate credit to the original author(s) and the source, provide a link to the Creative Commons license, and indicate if changes were made. The images or other third party material in this article are included in the article's Creative Commons license, unless indicated otherwise in a credit line to the material. If material is not included in the article's Creative Commons license and your intended use is not permitted by statutory regulation or exceeds the permitted use, you will need to obtain permission directly from the copyright holder. To view a copy of this license, visit <http://creativecommons.org/licenses/by/4.0/>.

This is a U.S. government work and not under copyright protection in the U.S.; foreign copyright protection may apply 2020